Hiroyuki Noda[1]
Research Scientist
Institute for Research on Earth Evolution,
Japan Agency for Marine-Earth
Science and Technology,
Yokohama, 236-0001, Japan
e-mail: hnoda@jamstec.go.jp

Nadia Lapusta
Professor of Mechanical Engineering
and Geophysics,
Division of Engineering and Applied Science,
Division of Geological and Planetary Sciences,
California Institute of Technology,
Pasadena, CA, 91125
e-mail: lapusta@its.caltech.edu

On Averaging Interface Response During Dynamic Rupture and Energy Partitioning Diagrams for Earthquakes

Earthquakes occur as dynamic shear cracks and convert part of the elastic strain energy into radiated and dissipated energy. Local evolution of shear strength that governs this process, which is variable in space and time, can be studied from laboratory experiments and rupture models. At the same time, increasingly accurate measurements of radiated energy and other quantities characterize earthquakes in a rupture-averaged way. Here, we present and study two approaches to averaging frictional dissipation during dynamic rupture. The first one is based on the actual progression of dissipation, but the associated averaged shear stress does not reflect the local friction behavior. The second one is constructed to preserve prevailing features of local stress-slip response and performs well in the examples studied. The developed approach should be useful for visualizing energy partitioning in dynamic models and linking them to observations using diagrams that reflect dominant features of local stress evolution. [DOI: 10.1115/1.4005964]

1 Introduction

Earthquakes, which are perceived as ground shaking, can be successfully modeled as dynamic shear cracks (also called ruptures) propagating on pre-existing frictional interfaces in the Earth's crust (e.g., Ref. [1] and references therein). These dynamic events occur as part of a wide range of slip phenomena on faults, including interseismic creep and slow slip events. Earthquakes can indeed be simulated in models that reproduce both seismic and aseismic fault phenomena, where they spontaneously result due to self-accelerating fault slip (e.g., Refs. [2–4]).

The success of models in reproducing a number of observed phenomena can be attributed, in large part, to our increasing understanding of the potential fault constitutive behavior through detailed laboratory and field studies of fault zones and their shear resistance (e.g., Refs. [5–12]). Such studies allow us to formulate increasingly sophisticated friction laws that include effects of populations of frictional contacts, shear heating, pore fluids, and other factors (e.g., Refs. [13–15]). The resulting fault descriptions, coupled with advanced numerical calculations, produce a variety of detailed earthquake source scenarios (e.g., Refs. [4,16]).

At the same time, due to the remote nature of observations and notorious difficulty of inverse problems, the most reliable quantitative data about many earthquakes often characterizes the rupture as a whole, e.g., through the total seismic moment, static stress drop (which is a measure of the average stress change), and various energy-related quantities (e.g., Ref. [17]). Hence it is important to develop rigorous ways of linking this averaged information to earthquake source models.

An important set of observable quantities are related to energy partitioning ([Refs. 18,19]). Earthquakes release some of the elastic strain energy stored in the crust by tectonic motion, converting part of the released energy into radiated energy E_R that causes the ground motion. The remaining part is dissipated during earthquake source processes, including frictional dissipation D and creation of inelastic deformation around the fault. If one assumes that friction is the dominating source of dissipation or, alternatively, that other sources of dissipation can be included in D through appropriately constructed friction laws, then the energy partitioning during earthquakes can be written as:

$$\Delta W = E_R + D \tag{1}$$

where ΔW is the decrease in the strain energy due to rupture. Note that D includes increased dissipation at the rupture tip due to concentrated stress, which is analogous to the "fracture energy" concept of singular elastic cracks. In this study, we will not separate "fracture energy," considering it as a part of the overall frictional dissipation D.

Improved estimates of radiated energy and other observable quantities can help constrain and understand fault behavior and earthquake physics. To facilitate such links, it would be useful to visualize fault dissipation and its relation to other energy-related quantities through appropriately averaged behaviors of shear stress with slip, which then can be used to illustrate energy partitioning, to establish relations between various averaged quantities, and to study the energy characteristics of different rupture models.

An example of a conceptual diagram of rupture-averaged behavior is shown in Fig. 1(*a*) (e.g., Ref. [17]), where the dissipation rate, which provides a measure of average shear stress, is assumed to evolve from its initial value τ^{ini} to its final value τ^{fin} with slip, following a linear slip-weakening profile (black solid line) often used in simulations of dynamic rupture for local friction behavior. Let A be the area of the ruptured region. If the initial and final values τ^{ini} and τ^{fin} are appropriately chosen, the striped trapezoid can be interpreted as the strain energy change per unit area of the fault, $\Delta W/A$, the gray area under the shear stress-slip curve provides dissipation density D/A, and their difference then corresponds to the radiation energy density, E_R/A. Note that the schematic diagram attempts to combine two desired properties: (i) the appropriate average relation between dissipative stress and slip that interprets various energy-related quantities as areas on the diagram, and (ii) the overall shape of the dissipative stress curve that resembles our ideas about the local frictional behavior (e.g., Fig. 1(*a*) incorporates the linear slip-weakening behavior).

[1]Corresponding author.

Contributed by the Applied Mechanics Division of ASME for publication in the JOURNAL OF APPLIED MECHANICS. Manuscript received December 23, 2011; final manuscript received January 22, 2012; accepted manuscript posted February 13, 2012; published online April 12, 2012. Editor: Robert M. McMeeking.

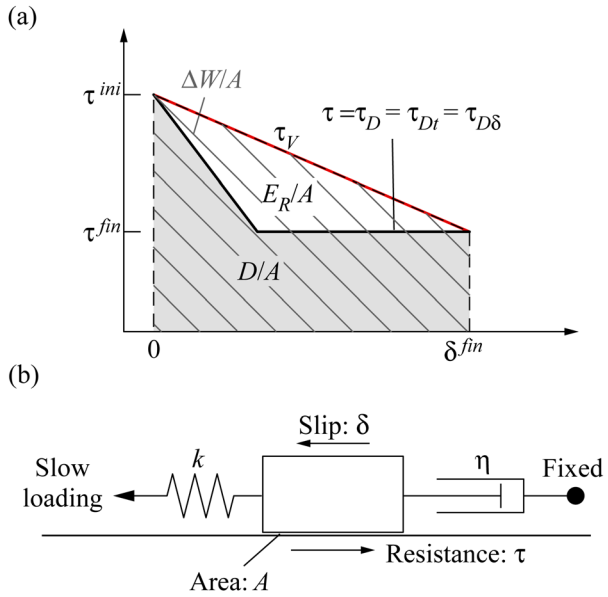

Fig. 1 (*a*) Schematic conceptual representation of energy partitioning per unit area during dynamic rupture, in which the change in strain energy ΔW goes into radiated energy E_R and frictional dissipation D. The issue is how to construct such a diagram that, at the same time, retains some information about the assumed local frictional behavior. (*b*) Schematics of a single-degree-of-freedom spring-slider system for which such diagram can be trivially constructed. In the system, the mass is ignored; the radiation is represented by a term proportional to slip rate of the block and illustrated on the diagram by a dashpot.

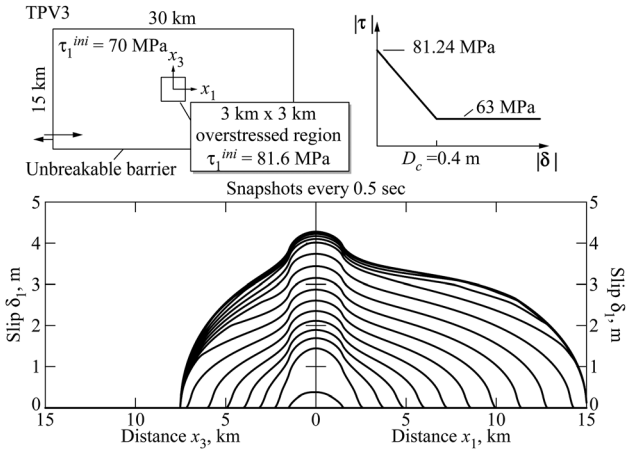

Fig. 2 An example of dynamic rupture on a planar interface embedded into a 3D elastic space. Top left: The rectangular rupture domain is prestressed to slip mostly in the x_1 direction, with an overstressed patch to initiate rupture. Top right: The assumed linear slip-weakening behavior on the interface that acts as a boundary condition to the elastodynamic equations in the bulk. Bottom: Slip accumulation every 0.5 s during dynamic rupture for two cross-sections of the rupture domain.

This leads to the following question: How do we rigorously combine properties (i) and (ii) in a single averaged diagram of a rupture process? Such a combination is trivially possible only for a one-degree-of-freedom system. An example is a spring-slider system which considers the motion of a rigid block on a frictional surface, pulled by an elastic spring (e.g., Ref. [20]), with the mass ignored and radiation represented by a term proportional to the slip rate of the block [21] (Fig. 1(*b*)). In such a system, the (local) frictional behavior between the block and the surface determines the (overall) dissipation rate, so that they are identically equal to each other.

However, dynamic rupture during earthquake is a spatially heterogeneous process, and thus the graphical representation of the energy partitioning (such as Fig. 1(*a*)) requires a proper averaging procedure. As an example, consider dynamic rupture on a planar fault embedded in a 3D elastic space, obtained as part of the SCEC/USGS Spontaneous Rupture Code Verification Project [22,23] (Fig. 2). The rupture occurs within a rectangular domain (Fig. 2, top-left panel) governed by linear slip-weakening friction (Fig. 2, top-right panel). The detailed problem description is given in Ref. [22]. The rupture is initiated by over-stressing a square region in the middle of the fault, and propagates spontaneously over the rectangular domain, until it reaches the unbreakable barriers that surround the domain and eventually cause the arrest of slip. The accumulation of slip every 0.5 s is illustrated in the bottom panel of Fig. 2, with the left side plotting the rupture progression in the Mode III direction (along the x_3 axis shown in the top-left panel) and the right side plotting the rupture progression in the Mode II direction (along the x_1 axis). Although the fault constitutive law is relatively simple, different points on the fault experience different shear stress and slip histories and different final slips. Averaging such a process, variable in space and time, to obtain a simple and useful energy partitioning diagram of the kind shown in Fig. 1(*a*) is not straightforward.

In the following, we consider averaging of such rupture processes and potential construction of energy-partitioning diagrams that preserve key features of local frictional behavior. In Secs. 2 and 3, we introduce a general problem setting and review the well-known concept of virtual work rate used to compute the strain energy change. In Sec. 4, we discuss the area-averaged dissipation rate, point out it does not capture the local evolution of frictional resistance, and then introduce an alternative construction of the dissipation rate that is based on the local frictional behavior. Sections 3–4 use the dynamic rupture of Fig. 2 to illustrate the concepts, and Sec. 5 provides additional examples.

2 Problem Setting for a Dynamic Rupture Process

Let us consider dynamic rupture on a planar interface S embedded in a linear elastic medium (Fig. 3). We denote the position vector spanning S by $\boldsymbol{x}$, components of vector quantities by subscripts 1, 2, and 3, and initial and final values by superscripts $^{\text{ini}}$ and $^{\text{fin}}$. For simplicity, we do not consider opening and interpenetration of the two sides of the interface so that the discontinuity in the particle displacement across S is restricted to the in-plane components and called "slip." The slip vector $\boldsymbol{\delta}$ is zero at the initial time $t = t^{\text{ini}} = 0$ everywhere on the interface and becomes nonzero in the rupture domain Σ of area A at the final time $t = t^{\text{fin}}$. The spatio-temporal slip distribution $\boldsymbol{\delta}(t, \boldsymbol{x})$ satisfies:

$$\boldsymbol{\delta}(0, \boldsymbol{x}) = \boldsymbol{0}, \quad \boldsymbol{\delta}(t^{\text{fin}}, \boldsymbol{x}) = \boldsymbol{\delta}^{\text{fin}}(\boldsymbol{x}) \tag{2}$$

where $\boldsymbol{\delta}^{\text{fin}}$ is the final slip distribution. Without loss of generality, we set Cartesian coordinates such that the interface is normal to $\boldsymbol{e_2}$ and the overall slip direction corresponds to $\boldsymbol{e_1}$:

$$\int_S \boldsymbol{\delta}^{\text{fin}} dS = A\bar{\delta}^{\text{fin}} \boldsymbol{e_1} \tag{3}$$

where $\bar{\delta}^{\text{fin}}$ is the average of the final slip distribution.

Note that individual points inside the rupture domain can have directions of final slip different from $\boldsymbol{e_1}$, necessitating projections onto $\boldsymbol{e_1}$ in several expressions that follow. In both rupture models as well as natural earthquakes, often there is a dominating slip direction, e.g., along the fault strike, with the other component being relatively minor.

The shear stress $\boldsymbol{\tau}$ on the interface depends on time and space, with the initial and final distributions given by:

$$\boldsymbol{\tau}(0, \boldsymbol{x}) = \boldsymbol{\tau}^{\text{ini}}(\boldsymbol{x}), \quad \boldsymbol{\tau}(t^{\text{fin}}, \boldsymbol{x}) = \boldsymbol{\tau}^{\text{fin}}(\boldsymbol{x}) \tag{4}$$

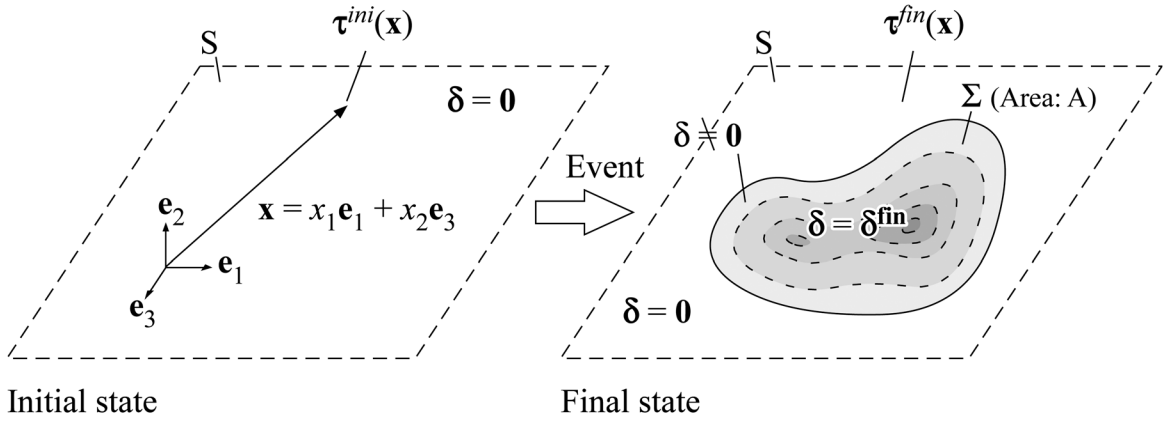

Fig. 3 Schematics of the initial and final states of a dynamic rupture process on a planar interface embedded into a 3D linear elastic space

Spatio-temporal dependency of $\boldsymbol{\tau}$ is derived from its initial value $\boldsymbol{\tau}^{\text{ini}}$ and spatio-temporal slip distribution $\boldsymbol{\delta}$ through standard elastodynamics equations (e.g., Ref. [1]). Note that shear stress still evolves after slip stops everywhere in the rupture domain, due to wave-mediated stress transfers. Hence t^{fin} is chosen so that the (wave-mediated) stress redistribution after t^{fin} is negligible in the vicinity of the rupture domain.

3 Strain Energy Change and Virtual Work Rate

From Eq. (1), one side of the energy balance is the decrease in strain energy, ΔW, caused by dynamic rupture and represented in the energy partitioning diagram by the area below the line of the virtual work rate. ΔW can be calculated by integrating the work rate along a virtual quasi-static process connecting the initial and final states (e.g., Ref. [17]), similarly to the case with a one-degree-of-freedom system. The initial and final distributions of slip and shear stress satisfy elastostatic equations, and so does any linear interpolation/extrapolation of them. Let us choose a virtual process along such linear interpolation, with slip $\delta_{vp}(\lambda, \boldsymbol{x})$ and shear stress $\tau_{vp}(\lambda, \boldsymbol{x})$ given by:

$$\begin{aligned}\boldsymbol{\delta}_{vp}(\lambda, \boldsymbol{x}) &= \lambda\boldsymbol{\delta}^{\text{fin}}(\boldsymbol{x}) \\ \boldsymbol{\tau}_{vp}(\lambda, \boldsymbol{x}) &= \lambda\boldsymbol{\tau}^{\text{fin}}(\boldsymbol{x}) + (1-\lambda)\boldsymbol{\tau}^{\text{ini}}(\boldsymbol{x})\end{aligned} \tag{5}$$

where λ is a parameter ranging from 0 to 1 and subscripts "vp" stand for "virtual process." Then ΔW can be written as:

$$\Delta W = \int_0^1 \frac{dW}{d\lambda} d\lambda = \int_0^1 \int_\Sigma \boldsymbol{\tau}_{vp} \cdot \frac{d\boldsymbol{\delta}_{vp}}{d\lambda} dS d\lambda \tag{6}$$

Using Eqs. (5) and (3), one can obtain the following expression for the strain energy change per unit rupture area in terms of virtual slip and stress quantities averaged over the ruptured domain:

$$\Delta W/A = \int_0^{\overline{\delta}^{\text{fin}}} \tau_V(\overline{\delta}_V) d\overline{\delta}_V \tag{7}$$

where $\overline{\delta}_V = \lambda\overline{\delta}^{\text{fin}}$ describes the evolution of average slip in the virtual quasi-static process (Eq. (5)) and τ_V is a linear function of $\overline{\delta}_V$ defined as:

$$\begin{aligned}\tau_V(\overline{\delta}_V) &= \frac{1-\overline{\delta}_V}{\overline{\delta}^{\text{fin}}} \frac{\int_\Sigma \boldsymbol{\tau}^{\text{ini}} \cdot \boldsymbol{\delta}^{\text{fin}} dS}{\int_\Sigma \boldsymbol{e_1} \cdot \boldsymbol{\delta}^{\text{fin}} dS} + \frac{\overline{\delta}_V}{\overline{\delta}^{\text{fin}}} \frac{\int_\Sigma \boldsymbol{\tau}^{\text{fin}} \cdot \boldsymbol{\delta}^{\text{fin}} dS}{\int_\Sigma \boldsymbol{e_1} \cdot \boldsymbol{\delta}^{\text{fin}} dS} \\ &= \frac{1-\overline{\delta}_V}{\overline{\delta}^{\text{fin}}} \frac{\int_\Sigma (\tau_1^{\text{ini}}\delta_1^{\text{fin}} + \tau_3^{\text{ini}}\delta_3^{\text{fin}}) dS}{\int_\Sigma \delta_1^{\text{fin}} dS} + \frac{\overline{\delta}_V}{\overline{\delta}^{\text{fin}}} \frac{\int_\Sigma (\tau_1^{\text{fin}}\delta_1^{\text{fin}} + \tau_3^{\text{fin}}\delta_3^{\text{fin}}) dS}{\int_\Sigma \delta_1^{\text{fin}} dS}\end{aligned} \tag{8}$$

The initial and final values of τ_V are:

$$\tau_V(0) = \frac{\int_\Sigma \boldsymbol{\tau}^{\text{ini}}(\boldsymbol{x}) \cdot \boldsymbol{\delta}^{\text{fin}}(\boldsymbol{x}) dS}{\int_\Sigma \boldsymbol{e_1} \cdot \boldsymbol{\delta}^{\text{fin}}(\boldsymbol{x}) dS} = \frac{\int_\Sigma (\tau_1^{\text{ini}}\delta_1^{\text{fin}} + \tau_3^{\text{ini}}\delta_3^{\text{fin}}) dS}{\int_\Sigma \delta_1^{\text{fin}} dS} \tag{9}$$

and

$$\tau_V(\overline{\delta}^{\text{fin}}) = \frac{\int_\Sigma \boldsymbol{\tau}^{\text{fin}}(\boldsymbol{x}) \cdot \boldsymbol{\delta}^{\text{fin}}(\boldsymbol{x}) dS}{\int_\Sigma \boldsymbol{e_1} \cdot \boldsymbol{\delta}^{\text{fin}}(\boldsymbol{x}) dS} = \frac{\int_\Sigma (\tau_1^{\text{fin}}\delta_1^{\text{fin}} + \tau_3^{\text{fin}}\delta_3^{\text{fin}}) dS}{\int_\Sigma \delta_1^{\text{fin}} dS} \tag{10}$$

respectively.

The function τ_V of Eq. (8) gives the virtual work rate. Figure 4 (solid line) shows an example of $\tau_V\overline{\delta}_V$ for the problem of Fig. 2. The area below the virtual work line in Fig. 2 gives the strain energy change per unit area, $\Delta W/A$, which can be computed as:

$$\Delta W/A = (\tau_V(0) + \tau_V(\overline{\delta}^{\text{fin}}))\overline{\delta}^{\text{fin}}/2 \tag{11}$$

Note that some complexity in the expressions of Eqs. (8)–(10), as well as in other averaged quantities introduced in the following sections, is caused by the possibility of different directions of final slip at different points of the rupture domain. The overall slip direction is parallel to $\boldsymbol{e_1}$ as set by Eq. (3), but individual points can have different final slip directions, necessitating the projection onto $\boldsymbol{e_1}$ that enters the expressions of Eqs. (8)–(10). If the directions of the final slip distribution $\boldsymbol{\delta}^{\text{fin}}(\boldsymbol{x})$ are the same for all points in the rupture domain Σ, i.e., $\delta_3^{\text{fin}} = 0$, the expressions of Eqs. (8)–(10) simplify to:

$$\begin{aligned}\tau_V(\overline{\delta}_V) &= \frac{1-\overline{\delta}_V}{\overline{\delta}^{\text{fin}}} \frac{\int_\Sigma \tau_1^{\text{ini}}\delta_1^{\text{fin}} dS}{\int_\Sigma \delta_1^{\text{fin}} dS} + \frac{\overline{\delta}_V}{\overline{\delta}^{\text{fin}}} \frac{\int_\Sigma \tau_1^{\text{fin}}\delta_1^{\text{fin}} dS}{\int_\Sigma \delta_1^{\text{fin}} dS} \\ \tau_V(0) &= \frac{\int_\Sigma \tau_1^{\text{ini}}\delta_1^{\text{fin}} dS}{\int_\Sigma \delta_1^{\text{fin}} dS}, \quad \tau_V(\overline{\delta^{\text{fin}}}) = \frac{\int_\Sigma \tau_1^{\text{fin}}\delta_1^{\text{fin}} dS}{\int_\Sigma \delta_1^{\text{fin}} dS}\end{aligned} \tag{12}$$

In this case, the initial and final values of τ_V are the weighted averages, with the final slip distribution $\delta^{\text{fin}}(\boldsymbol{x})$ as the weighting function, of the initial ($\tau^{\text{ini}}(\boldsymbol{x})$) and final ($\tau^{\text{fin}}(\boldsymbol{x})$) shear stress distributions, respectively. The formulae (Eq. (12)) would be approximately valid for cases where deviations from the overall

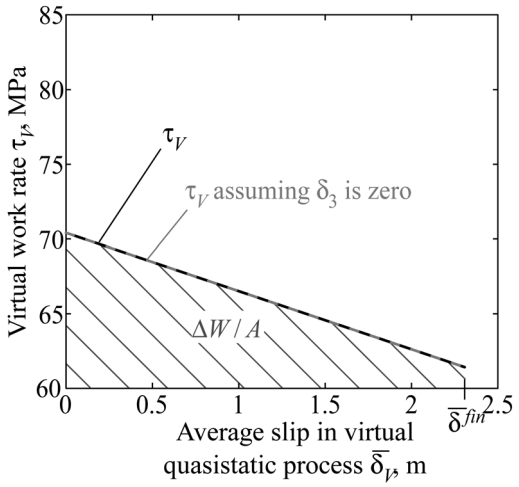

Fig. 4 Illustration of the virtual work rate and the strain energy change for the case of Fig. 2 The exact virtual work rate calculated using Eq. (8) is plotted as the black solid line. The approximate rate from Eq. (12), which assumes the same direction of final slip for all ruptured points (gray dashed line), is indistinguishable from the exact one on this scale, for reasons discussed in the text.

slip direction are not significant in individual points. Consider the case of Fig. 2 as an example. The initial shear stress is in the direction $\boldsymbol{e_1}$, resulting in the final slip being close to that direction in all points, with some (much smaller) slip component in the direction $\boldsymbol{e_3}$ in the corners of the ruptured domain. In the example of Fig. 2, using the simplified Eq. (12) results in the virtual work rate indistinguishable on the scale of Fig. 4 from the exact calculation based on Eq. (8).

4 Average Dissipation Rate Functions During Dynamic Rupture

An important ingredient of the energy partitioning diagrams is the average dissipative behavior of the rupture domain per unit area (the solid black line in Fig. 1(*a*)), plotted as the evolution of a dissipative stress-like quantity (that represents an averaging of shear stress) with an average measure of slip. During dynamic rupture, the evolution of shear stress with slip, and the final value of slip, depends, in general, on the location in the rupture domain. Therefore, the construction of averaged shear stress evolution with slip that would be suitable for visualizing the energy partitioning is not trivial. The main requirement is for the resulting average dissipative stress $\bar{\tau}_D$ to reflect the total dissipation on the fault D per unit area through:

$$D/A = \int_0^{\bar{\delta}^{\text{fin}}} \tau_D(\delta) d\delta \tag{13}$$

In the following, we present two ways of constructing such a function. The first one is more straightforward, as it represents the actual progression of the dissipation in the rupture process. However, the resulting averaged shear stress does not resemble the typical local evolution of shear stress with slip. The second one is designed to retain that local information.

4.1 Time Evolution of Fault-Averaged Dissipation and the Associated Dissipative Stress. Dissipation in the rupture domain accumulates monotonically and reaches the maximum value D at the end of the rupture process. Hence it is natural to consider the evolution of dissipation with time, or, equivalently, with slip averaged over the ruptured domain. The associated dissipative stress function would allow to visualize, for example, at what stages of the rupture process significant dissipation takes place. The total dissipation on the fault can be written as:

$$D = \int_0^{t^{\text{fin}}} \int_S \boldsymbol{\tau} \cdot \dot{\boldsymbol{\delta}} dS dt \tag{14}$$

where $\dot{\boldsymbol{\delta}}$ is slip rate on the fault, a time derivative of slip $\boldsymbol{\delta}$. Let us change the integration variable from time to average slip using:

$$dt \int_S \boldsymbol{e}_1 \cdot \dot{\boldsymbol{\delta}} dS = d\bar{\delta}_1 \, A = dP_1 \tag{15}$$

where $\bar{\delta}_1$ is the component of slip in the overall slip direction $\boldsymbol{e_1}$ averaged over the rupture domain and P_1 is the component of the potency vector in the overall slip direction $\boldsymbol{e_1}$. Note that $\bar{\delta}_1$ is assumed to increase with time, which holds for the vast majority if not all of the rupture models. Then Eq. (14) leads to:

$$D = A \int_0^{\bar{\delta}^{\text{fin}}} \tau_{Dt}(\bar{\delta}_1) d\bar{\delta}_1 \tag{16}$$

where

$$\tau_{Dt}(\bar{\delta}_1) = \frac{\int_S \boldsymbol{\tau} \cdot \dot{\boldsymbol{\delta}} dS}{\int_S \boldsymbol{e_1} \cdot \dot{\boldsymbol{\delta}} dS} = \frac{\int_S (\tau_1 \dot{\delta}_1 + \tau_3 \dot{\delta}_3) dS}{\int_S \dot{\delta}_1 dS} \tag{17}$$

The average dissipative stress τ_{Dt} defined by Eq. (17) represents the increment of dissipation per unit increment of potency in the overall slip direction $\boldsymbol{e_1}$. As Eq. (16) clearly shows, the area below its plot versus average slip $\bar{\delta}_1$ amounts to the total dissipation per unit area, as desired for the energy partitioning diagrams. If the slip rate $\dot{\boldsymbol{\delta}}$ is parallel to the overall final slip direction everywhere on the fault at all times, i.e., $\dot{\delta}_3 = 0$ (or close to that scenario), τ_{Dt} can be interpreted as the weighted average of shear stress distribution on the fault, with the slip rate as the weighting function. The initial and final values of τ_{Dt}, τ_{Dt} (0) and $\tau_{Dt}(\bar{\delta}^{\text{fin}})$, are dominated by shear stresses in regions of higher slip rate at the initiation and termination of rupture.

As an example, let us consider the dissipative stress τ_{Dt} computed for the case of Fig. 2 and shown in Fig. 5(*a*) and 5(*b*) as a function of time and average slip, respectively. As expected, τ_{Dt} reflects the time-dependent behavior of the dynamic rupture. In Figs. 5(*a*) and 5(*b*), the initial value of τ_{Dt} corresponds to the assigned shear stress value on the overstressed initial patch; the subsequent rapid drop-off describes the rapid evolution of shear stress on the patch and rupture spread into the surrounding areas of lower prestress; and two sharp changes in the curve indicated by arrows occur when the rupture reaches the unbreakable barriers that surround the fault, which send out arrest fronts and decrease the slip rate and hence the dissipative stress. It should be emphasized that the dependence of τ_{Dt} on average slip (Fig. 5(*b*)) is quite different from the local friction behavior (dashed line in Fig. 5(*b*)).

One might be tempted to consider another, relatively simple, unweighted average, which is just the spatial average of shear stress distribution $\boldsymbol{\tau}(t, \boldsymbol{x})$ in the overall slip direction given by:

$$\bar{\tau}_1 = \frac{\int_S \tau_1 dS}{A} \tag{18}$$

Figures 5(*c*) and 5(*d*) show $\bar{\tau}_1$ for the case of Fig. 2 plotted against time and average slip, respectively. Although $\bar{\tau}_1$ is probably the most straightforward definition of the average shear stress, it does not appear to be a useful one: (i) it cannot be used for visualizing energy partitioning during a dynamic rupture, since the area below

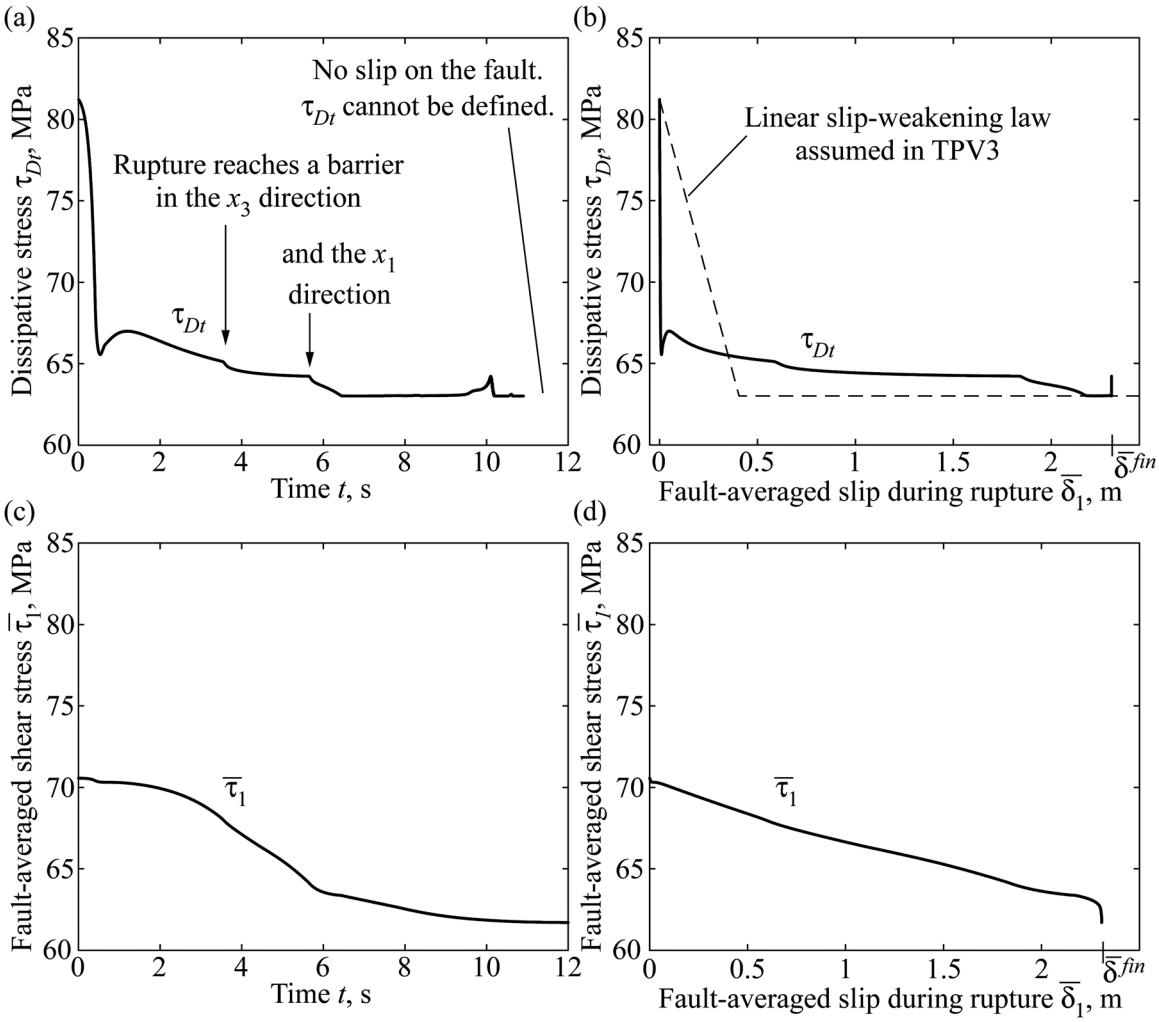

Fig. 5 (*a*)-(*b*) Average dissipative shear stress τ_{Dt} on the fault from Eq. (17) for the rupture case of Fig. 2, plotted as a function of time in (*a*) and average slip in (*b*). Note that τ_{Dt} is quite different from the linear slip-weakening friction behavior experienced by each point on the fault (dashed line in (*b*)). (*c*)–(*d*) Rupture area-averaged shear stress $\bar{\tau}_1$ plotted against time in (*c*) and slip in (*d*). This relatively simple area-averaging of shear stress is different from both the dissipative stress τ_{Dt} and the assigned local friction behavior. $\bar{\tau}_1$ does not integrate to the total dissipation, and hence it cannot be used in the energy partitioning diagrams.

$\bar{\tau}_1$ plotted against $\bar{\delta}_1$ is not equal to the total dissipation per area D/A, and (ii) it does not resemble, and hence cannot be used to visualize, the local friction behavior.

4.2 Average Dissipation Rate Function Based on Local Friction Behavior. The average shear stress versus slip behavior that represents dissipation in energy-partitioning diagrams is typically assumed to follow the local friction behavior (e.g., Ref. [17]). In fact, the canonical diagram of Fig. 1(*a*) is intended to capture the decrease of friction at each point from a peak to near-constant dynamic value. Such representation of energy partitioning would be quite useful, as it could involve, and potentially test against observations, different ideas about friction, either from theories or from laboratory experiments which essentially explore local friction behavior. Such representation would also allow to systematically study energy balance issues in simulations of dynamic rupture and their comparison with laboratory experiments. However, the dissipation function τ_{Dt} defined in Eq. (17) can be substantially different from the evolution of shear stress at a point on the fault during dynamic rupture, as discussed in the previous subsection.

Thus it is useful to find another averaging procedure over the entire fault that attempts to preserve the shape of the local shear stress evolution with slip. Note that such preservation would only be possible if the behavior of different fault points has similarities, as in the example of Fig. 2, in which all points are governed by linear slip-weakening behavior; if the constitutive response of the slipping interface is so complex that local shear stress-slip histories are conceptually different for different points, then there is no typical local behavior for the averaging to capture.

We propose the following approach to creating such an average stress-slip function $\tau_{D\delta}(\delta_1')$, which is defined for $0 < \delta_1' < \bar{\delta}^{\text{fin}}$ and can be used as $\tau_D(\delta)$ in Eq. (13). The key steps are: (i) At each point $\boldsymbol{x}$ on the fault, construct the dependence of the (scalar) dissipative stress τ_{sc} on (scalar) slip δ_1 that reproduces dissipation density. In principle, this is just the local shear stress behavior with slip, with a complication due to the fact that both shear stress and slip are vectors with potentially changing directions, and the scalar version of that needs to preserve dissipation. An example of this step for problem TPV3 of Fig. 2 is shown in the top row of Fig. 6. (ii) At each point $\boldsymbol{x}$ on the fault, stretch/compress the resulting dependence along the slip axis to adjust the local final slip to the overall final fault-averaged slip $\bar{\delta}^{\text{fin}}$; the resulting new slip variable is denoted by δ_1'. To preserve the dissipation density at each point given by the area under the stress-slip curve, compensate by compressing/stretching the dependence along the stress

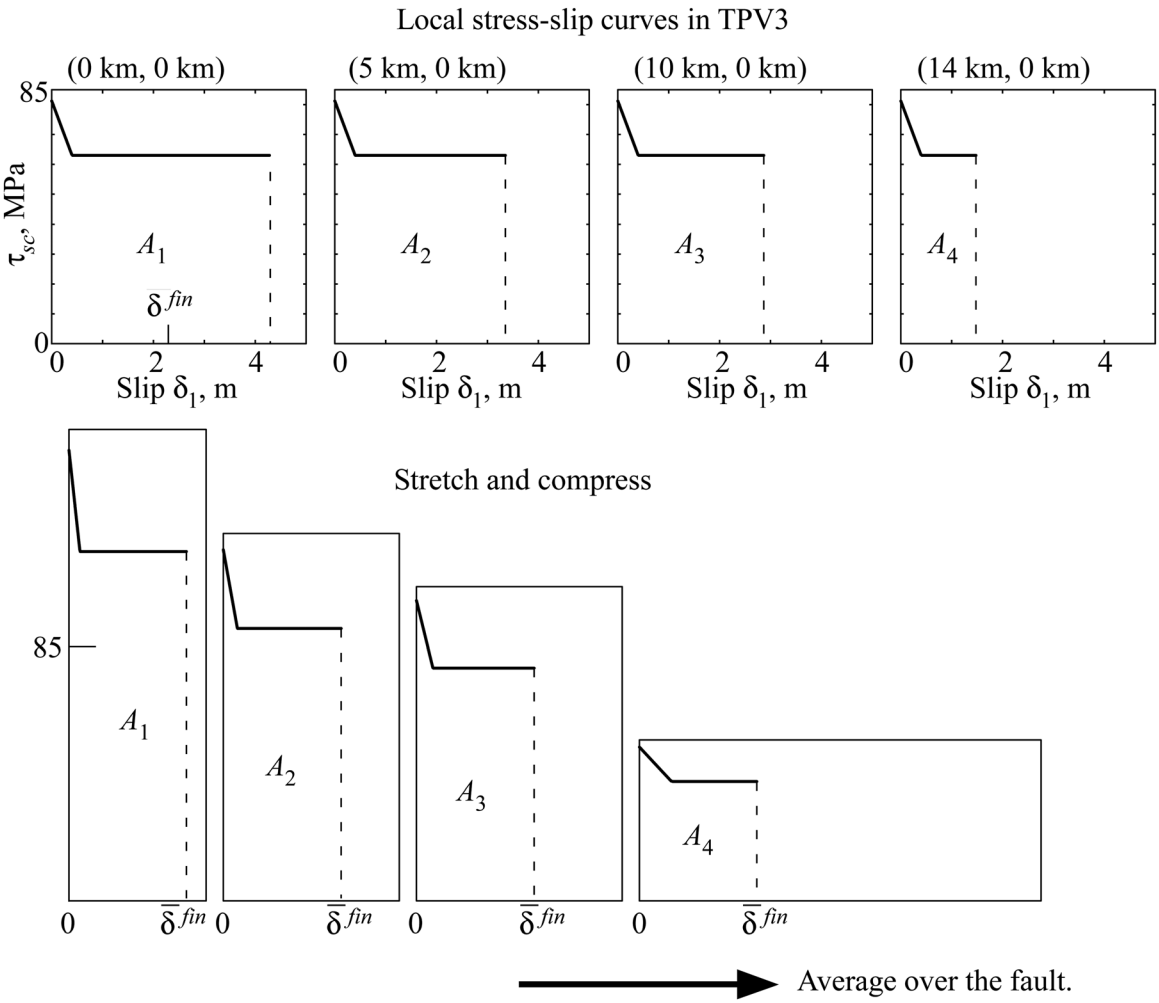

Fig. 6 Illustration of steps in constructing average dissipation stress based on local friction behavior, using the case of Fig. 2 as an example. (Top row) Local scalar dependence of dissipative stress on slip. (Bottom row) The local dependence is stretched/compressed along the slip axis to adjust the local final slip values to the overall fault-averaged final slip $\overline{\delta}^{\text{fin}}$, and then compressed/stretched along the stress axis to keep the same area (A_1 to A_4) under the curves and hence the same dissipation density.

axis. At this point, all local dissipation functions are defined with respect to the same slip variable δ_1', with $0 < \delta_1' < \overline{\delta}^{\text{fin}}$. An example of this step is shown in the bottom row of Fig. 6. (iii) For each value of δ_1', take the spatial average of the rescaled shear stress over the rupture domain Σ.

The resulting fault-averaged function $\tau_{D\delta}(\delta_1')$, $0 < \delta_1' < \overline{\delta}^{\text{fin}}$, for the example of Fig. 6 is shown in Fig. 7. Unlike the dissipative shear stress τ_{D}, $\tau_{D\delta}(\delta_1')$ resembles the local linear slip-weakening relation, at least in the present example which is a relatively simple dynamic rupture. Note that the averaging also introduces some differences, as expected. For example, the relation between local shear stress and local slip has a sharp change in slope at $\delta = 0.4$ m, but the averaging procedure (Fig. 6) results in a smooth slope change. More examples of the results of this averaging procedure are provided in Sec. 5.

We now give the mathematical expressions for the steps (i)-(iii). Let us assume that the component of slip vector $\boldsymbol{\delta}$ parallel to the overall slip direction, δ_1, is an increasing function of time t everywhere on the fault. Then there is an inverse function $t_{\text{inv}}(\hat{\delta}_1, \boldsymbol{x})$ for $0 < \hat{\delta}_1 < \boldsymbol{\delta}^{\text{fin}}(\boldsymbol{x}) \cdot \boldsymbol{e_1} = \delta_1^{\text{fin}}(\boldsymbol{x})$ that gives the time at which point $\boldsymbol{x}$ reaches slip $\hat{\delta}_1$ in the overall slip direction $\boldsymbol{e_1}$:

$$\delta_1(t_{\text{inv}}(\hat{\delta}_1, \boldsymbol{x}), \boldsymbol{x}) = \hat{\delta}_1 \quad \text{for all} \quad 0 < \hat{\delta}_1 < \delta_1^{\text{fin}}(\boldsymbol{x}) \tag{19}$$

Now the dissipation area-density per unit time Ω can be written as a function of δ_1 through:

$$\Omega(\delta_1, \boldsymbol{x}) = \boldsymbol{\tau}(t_{\text{inv}}(\delta_1, \boldsymbol{x}), \boldsymbol{x}) \cdot \dot{\boldsymbol{\delta}}(t_{\text{inv}}(\delta_1, \boldsymbol{x}), \boldsymbol{x}) \tag{20}$$

The total dissipation is given by:

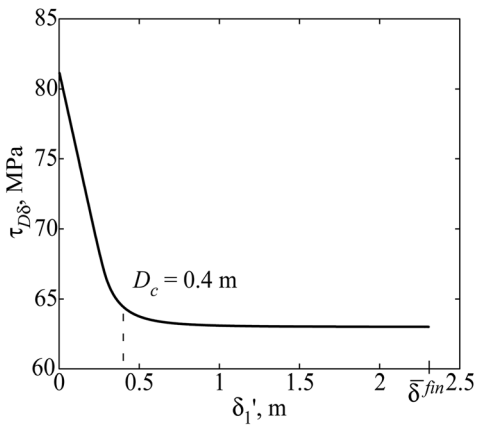

Fig. 7 Average dissipation stress based on local friction behavior, $\tau_{D\delta}(\delta_1')$. This function of average stress versus slip can be used in the energy partitioning diagram of the type Fig. 1(*a*).

$$D = \int_S \int_0^{t^{\text{fin}}} \Omega(\delta_1(t, \boldsymbol{x}), \boldsymbol{x}) dt dS \tag{21}$$

By changing the integration variable to slip, we get:

$$D = \int_S \int_0^{\delta_1^{\text{fin}}(\boldsymbol{x})} \frac{\Omega(\delta_1, \boldsymbol{x})}{\dot{\delta}_1(\delta_1, \boldsymbol{x})} d\delta_1 dS \tag{22}$$

where $\dot{\delta}_1(\delta_1, \boldsymbol{x})$ is the component of the slip rate vector $\dot{\boldsymbol{\delta}}(t_{\text{inv}}(\delta_1, \boldsymbol{x}), \boldsymbol{x})$ in the overall slip direction. Note that the integrand in Eq. (22) is precisely the local scalar dependence τ_{sc} of dissipative stress on slip discussed in step (i) above.

Now we would like to adjust the integration with respect to slip to be from zero to the final average slip $\overline{\delta}^{\text{fin}}$. To that end, we introduce a rescaled integration variable $\delta_1' = \delta_1/\tilde{\delta}_1(x)$, where $\tilde{\delta}_1(\boldsymbol{x}) = \delta_1^{\text{fin}}(\boldsymbol{x})/\overline{\delta}^{\text{fin}}$. As δ_1 varies from 0 to the final slip $\delta_1^{\text{fin}}(\boldsymbol{x})$ at the location $\boldsymbol{x}$, the rescaled variable δ_1' varies from 0 to the final fault-averaged slip $\overline{\delta}^{\text{fin}}$. From Eq. (22), we obtain:

$$D = \int_S \int_0^{\overline{\delta}^{\text{fin}}} \frac{\Omega(\delta_1' \tilde{\delta}_1(\boldsymbol{x}), \boldsymbol{x})}{V_1(\delta_1' \tilde{\delta}_1(\boldsymbol{x}), \boldsymbol{x})} \frac{\delta_1^{\text{fin}}}{\overline{\delta}^{\text{fin}}} d\delta_1' dS \tag{23}$$

Note that the integrand in Eq. (23) is precisely the rescaled local scalar dependence of dissipative stress on slip discussed in step (ii) above. Now we can change the order of integration:

$$D = \int_0^{\overline{\delta}^{\text{fin}}} \int_S \frac{\Omega(\delta_1' \tilde{\delta}_1(\boldsymbol{x}), \boldsymbol{x})}{V_1(\delta_1' \tilde{\delta}_1(\boldsymbol{x}), \boldsymbol{x})} \frac{\delta_1^{\text{fin}}}{\overline{\delta}^{\text{fin}}} dS d\delta_1' \tag{24}$$

Because $\overline{\delta}^{\text{fin}}$ is the spatial average of slip and independent of $\boldsymbol{x}$, Eq. (24) can be rewritten as:

$$D = A \int_0^{\overline{\delta}^{\text{fin}}} \frac{\int_S \left(\Omega(\delta_1' \tilde{\delta}_1(\boldsymbol{x}), \boldsymbol{x}) / V_1(\delta_1' \tilde{\delta}_1(\boldsymbol{x}), \boldsymbol{x}) \right) \delta_1^{\text{fin}} dS}{\int_S \delta_1^{\text{fin}} dS} d\delta_1' \tag{25}$$

Comparing Eqs. (13) and (25), we define:

$$\bar{\tau}_{D\delta}(\delta_1') = \frac{\int_S \left(\Omega(\delta_1' \tilde{\delta}_1(\boldsymbol{x}), \boldsymbol{x}) / V_1(\delta_1' \tilde{\delta}_1(\boldsymbol{x}), \boldsymbol{x}) \right) \delta_1^{\text{fin}} dS}{\int_S \delta_1^{\text{fin}} dS} \tag{26}$$

where $\bar{\tau}_{D\delta}$ is a stress function which preserves overall dissipation as well as characteristics of the local shear stress as a function of local slip, at least for relatively simple rupture scenarios, as demonstrated later.

If the slip and slip rate on the fault are always parallel to the overall slip direction, $\bar{\tau}_{D\delta}$ can be written as:

$$\bar{\tau}_{D\delta}(\delta_1') = \frac{\int_S \tau_1(\delta_1' \tilde{\delta}_1(\boldsymbol{x}), \boldsymbol{x}) \delta_1^{\text{fin}} dS}{\int_S \delta_1^{\text{fin}} dS} \tag{27}$$

where $\tau_1(\delta_1' \tilde{\delta}_1(\boldsymbol{x}), \boldsymbol{x}) = \tau_1(\delta_1, \boldsymbol{x})$ is the shear stress which is parallel to the overall slip direction at a location $\boldsymbol{x}$. The averaging procedure discussed in steps (i)–(iii) and illustrated in Fig. 6 is clearer in this expression, which does not have the additional complexity caused by the potential deviations of the local slip process from the overall (final) slip direction $\boldsymbol{e_1}$.

4.3 Energy Partitioning Diagrams. We have defined the virtual work rate $\tau_V(\overline{\delta}_V)$ that allows us to visualize the strain energy change and two dissipation rate functions that are, essentially, average measures of dissipative shear stresses, $\tau_{Dt}(\overline{\delta}_1)$ and $\tau_{D\delta}(\delta_1')$. Using these two functions, we can represent the energy partitioning diagram in two ways. Let us illustrate them using the case of Fig. 2 as an example; the two diagrams are shown in Fig. 8. In both diagrams, the striped area below the virtual work rate $\tau_V(\overline{\delta}_V)$ (the slid straight line) is the decrease in elastic strain energy per fault area $\Delta W/A$, and the gray areas below $\tau_{Dt}(\overline{\delta}_1)$ and $\tau_{D\delta}(\delta_1')$ both indicate the dissipation on the fault per unit area D/A. The radiated energy E_R/A can be obtained as the difference between $\Delta W/A$ and D/A, which pictorially corresponds to the combination of the areas indicated on the diagrams.

The functions plotted in the energy partitioning diagrams of Fig. 8 have different arguments, and hence the horizontal axes are used for different quantities (all of which range from 0 to $\overline{\delta}^{\text{fin}}$). For $\tau_V(\overline{\delta}_V)$, the horizontal axis tracks $\overline{\delta}_V$, the fault-averaged slip during the quasi-static virtual process which linearly connects the initial and final fault state. For $\tau_{Dt}(\overline{\delta}_1)$, the horizontal axis tracks $\overline{\delta}_1$, which gives the progression of the fault-averaged slip in a dynamic rupture process projected onto the overall direction of final slip. For $\tau_{D\delta}(\delta_1')$, the quantity δ_1' on the horizontal axis δ_1' represents the rescaled slip that makes the dissipative stress versus slip curve at each point extend from 0 to the final rupture area-

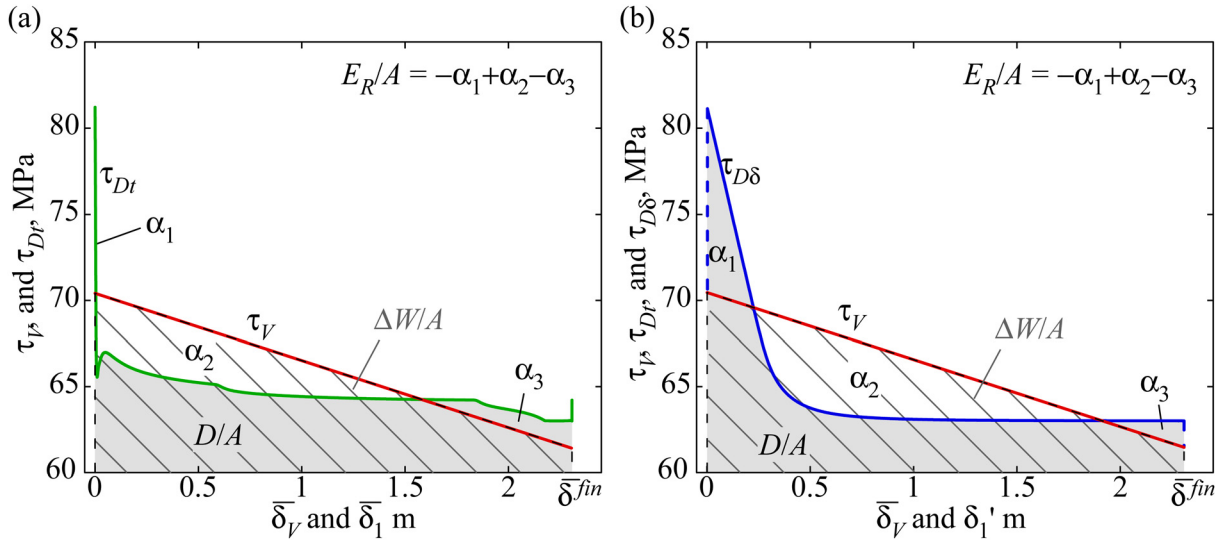

Fig. 8 Energy partitioning diagrams for the dynamic rupture of (Fig. 2) with (*a*) τ_{Dt} and (*b*) $\tau_{D\delta}$. $\Delta W/A$ and D/A are given by the striped and gray areas, respectively. E_R/A is the difference between them.

averaged slip $\bar{\delta}^{\text{fin}}$. Because of these differences between the arguments of the plotted quantities, it is not meaningful, for example, to take vertical cross-sections through these diagrams and compare the values of different quantities plotted to each other. Rather, these diagrams are useful in visualizing the dissipative behavior of the fault and the different energy-related quantities as areas.

Note that the values of functions τ_V, τ_{Dt}, and $\tau_{D\delta}$ at their endpoints (given by 0 and $\bar{\delta}^{\text{fin}}$) are, in general, different, as they represent different weighted averages of the initial and final stress distributions on the fault, with some important exceptions. Let us first compare τ_V and τ_{Dt}. Since they involve weighting of shear stress components by final slip for τ_V and slip rate distributions for τ_{Dt}, we expect their values at endpoints to be different for all but special cases (e.g., identically zero shear stress distributions), and they indeed are different in Fig. 8(*a*). Now consider the endpoints of τ_V and $\tau_{D\delta}$. For simplicity, let us concentrate on the case in which one direction of slip, $\boldsymbol{e_1}$, dominates (and slip and hence slip rate in the direction $\boldsymbol{e_3}$ is negligible). The initial and final values of $\tau_{D\delta}$ corresponds to averages of the initial and final values of the shear stress as a function of slip $\tau_1(\delta_1, \boldsymbol{x})$. If the points on the fault are constrained against any slip before the local shear stress reaches a given threshold (e.g., static friction), then $\tau_1(0, \boldsymbol{x})$ is equal to that threshold everywhere on the fault. Therefore, $\tau_{D\delta}(0)$ becomes the average of the threshold shear stress with the final local slip δ_1^{fin} as the weighting function. A similar discussion applies to the final value; $\tau_{D\delta}(\bar{\delta}^{\text{fin}})$ becomes the average of the sliding shear stress at the termination of slip. This is the case for the example considered in this section (Fig. 8(*b*)), and the endpoints are then not equal to those of τ_V. On the other hand, if the slip rate on the fault is nonzero as long as nonzero shear stress is applied (as occurs, for example, in simulations with rate- and state-dependent friction laws), then the initial value of local shear stress as a function of slip $\tau_1(0, \boldsymbol{x})$ is the initial shear stress $\tau_1^{\text{ini}}(\boldsymbol{x})$. In this case, the initial value of $\tau_{D\delta}$ is the average of initial shear stress τ_1^{ini} with the final slip as the weighting function, which is identical to the initial value of the virtual work rate $\tau_V(0)$. Similarly, the final value $\tau_{D\delta}(\bar{\delta}^{\text{fin}})$ is equal to $\tau_V(\bar{\delta}^{\text{fin}})$. An example of such behavior is shown in Sec. 5.2.

If the fault has uniform shear stress and uniform slip during an event, which is possible only in the one-degree-of-freedom system such as the one illustrated in Fig. 1, both diagrams would be identical to each other. In that sense, both diagrams are generalizations of the energy-partitioning diagram for a system with one degree of freedom.

5 Illustrating the Presented Fault-Averaged Relations Using Three Different Rupture Models

5.1 Self-Similar Singular Crack With Constant Stress Drop. Let us consider a 2D anti-plane singular crack which propagates with a constant rupture speed v_R and then abruptly arrests (Fig. 9(*a*)), a problem which has an analytical solution. For simplicity, we consider the shear stress on the fault to be initially uniform, $\boldsymbol{\tau}^{\text{ini}} = \tau^{ini}\boldsymbol{e_1}$, and the crack to be stress-free behind the crack tip, so that the constant stress drop is equal to τ^{ini}. During dynamic rupture propagation, the fault slip $\boldsymbol{\delta} = \delta_1 \boldsymbol{e_1}$ is given by [24]:

$$\delta_1(x_3, t) = \frac{1}{E\left(\sqrt{1 - v_R^2/c_s^2}\right)} \frac{\tau^{\text{ini}}}{\mu} \sqrt{(v_R t)^2 - x_3^2} \tag{28}$$

where E is the complete elliptic integral of the second kind, μ is the shear modulus, and c_s is the shear wave speed. When the rupture abruptly arrests at $t = t^{\text{arr}} = l/v_R$, the slip profile is:

$$\delta_1(x_3, t^{\text{arr}} = l/v_R) = \frac{1}{E\left(\sqrt{1 - v_R^2/c_s^2}\right)} \frac{\tau^{\text{ini}}}{\mu} \sqrt{l^2 - x_3^2} \tag{29}$$

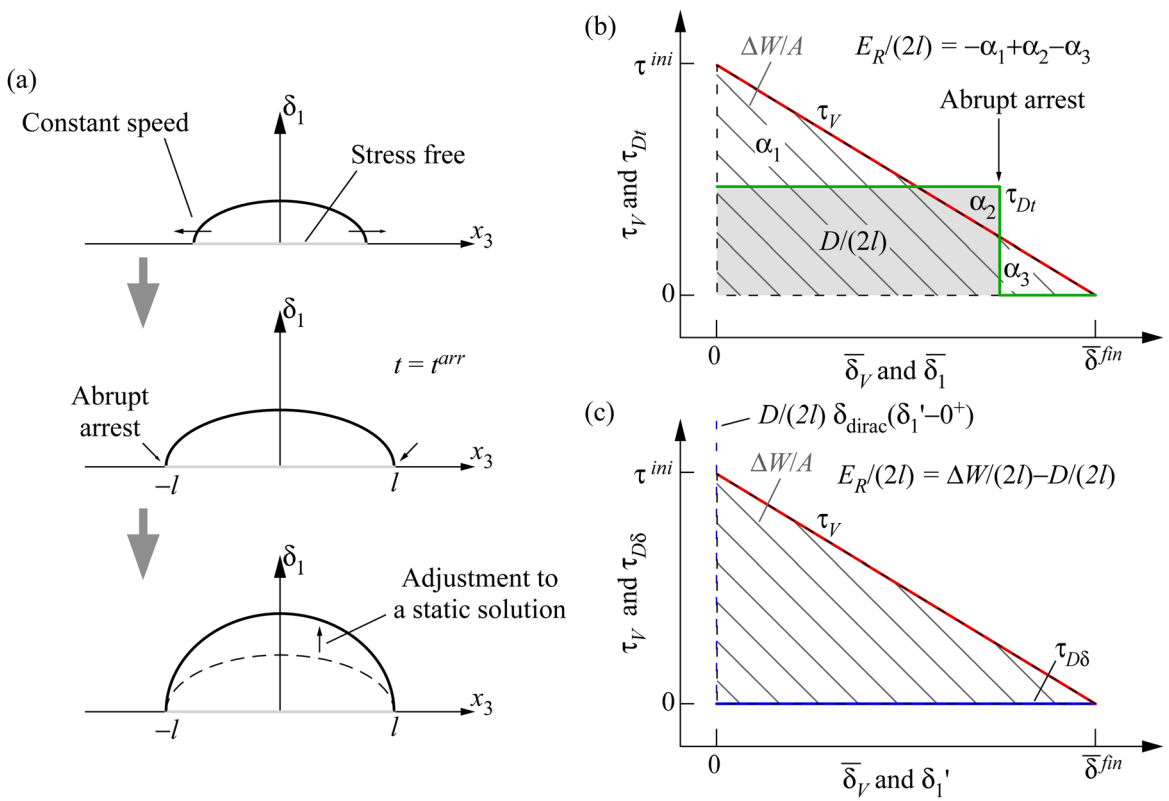

Fig. 9 (*a*) A dynamic process in which a singular Mode III crack propagates with a constant rupture speed V_R and then abruptly arrests. (*b*) Energy partitioning diagram for this example.

The subsequent wave-mediated stress redistribution leads to an adjustment of slip to the final (static) profile given by

$$\delta_1(x_3, t^{\text{fin}}) = \frac{\tau^{\text{ini}}}{\mu}\sqrt{l^2 - x_3^2} \tag{30}$$

In this case, we can determine the energy partitioning analytically. Since the rupture is 2D, the energy quantities, strain energy decrease ΔW and dissipation D, are measured per unit thickness of the fault in this section. Because the ruptured area is stress-free, the dissipation consists only of the energy flux to the rupture front:

$$G = G_0 w_{III}(v_R/c_s) = \frac{\pi(\tau^{\text{ini}})^2 v_R t}{2\mu} w_{III}(v_R/c_s) \tag{31}$$

where G_0 is the energy release rate in quasi-static rupture propagation and w_{III} is a function of the rupture speed [25]. Note that no energy is dissipated on the fault after the rupture is arrested at $t = t^{\text{arr}}$. The strain energy decrease can be calculated by integration of G_0 for a quasi-static rupture propagation:

$$\Delta W = \int_0^l G_0 d(v_R t) = \frac{\pi}{4}\frac{\tau^{\text{ini}}}{\mu}(\tau^{\text{ini}} l^2) \tag{32}$$

Both initial and final shear stress distributions over the final ruptured region Σ are uniform, with the values of τ^{ini} and 0, respectively. Therefore, the endpoints τ_V (0) and $\tau_V(\bar{\delta}^{\text{fin}})$ of the virtual work rate τ_V are equal to τ^{ini} and 0, respectively, with the average final slip $\bar{\delta}^{\text{fin}}$ given by:

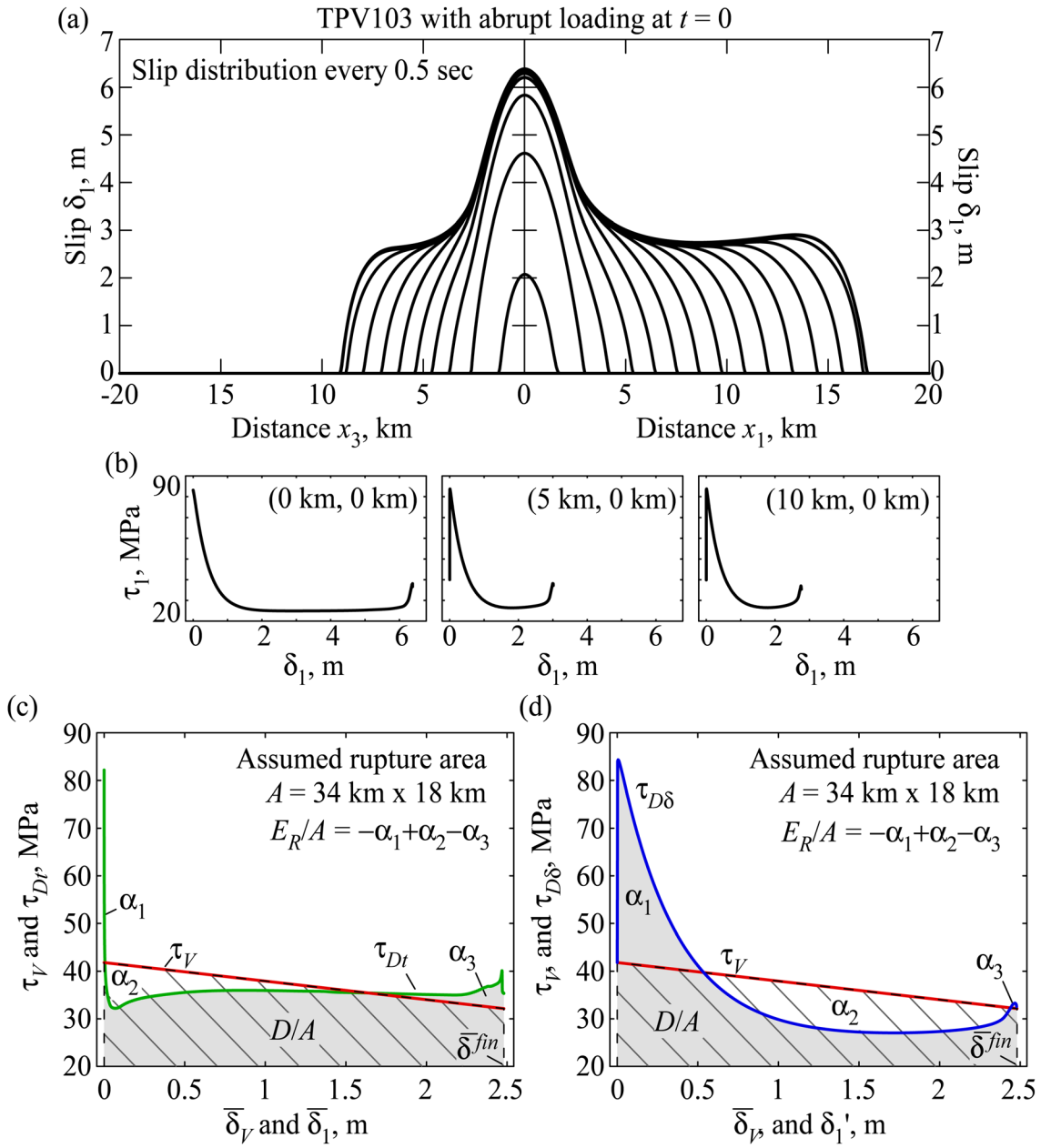

Fig. 10 (*a*) **Spatio-temporal distribution of slip in a pulse-like rupture scenario. The rupture occurs in a rectangular domain as illustrated in Fig. 2. The left part of the panel shows the rupture propagation in the Mode III direction and the right part of the panel shows the rupture propagation in the Mode II direction. (*b*) Local evolution of shear stress with slip at several points on the fault. (*c*)–(*d*) Fault-averaged rupture behavior using τ_{Dt} in (*c*) and $\tau_{D\delta}$ in (*d*). Note that the dissipation rate curve $\tau_{D\delta}$ reproduces the main features of the local behavior.**

$$\bar{\delta}^{\text{fin}} = \frac{\pi}{4}\frac{\tau^{\text{ini}}}{\mu} l \tag{33}$$

The area below τ_V is equal to the decrease in the strain energy per unit fault length $\Delta W/(2l)$, as expected. The total dissipation is given by:

$$D = \Delta W w_{III}(v_R/c_s) = \int_0^a G_0 d(v_R t) = \frac{\pi}{4}\frac{\tau^{\text{ini}}}{\mu}(\tau^{\text{ini}} l^2) w_{III}(v_R/c_s) \tag{34}$$

Let us consider the two average dissipative stresses, τ_{Dt} and $\tau_{D\delta}$, presented in Sec. 4.2. Dissipation per unit extension of the rupture (energy release rate) increases linearly with the rupture length $v_R t$ and thus with time t. Potency (and thus fault-averaged slip $\bar{\delta}_1$) is proportional to $(v_R t)^2$ and thus t^2, and the potency rate is proportional to time. Therefore τ_{Dt}, given by dissipation rate per potency rate, is independent of time during rupture propagation and becomes zero after the rupture is arrested:

$$\tau_{Dt} = \begin{cases} \tau^{\text{ini}} w_{III}(v_R)/2 & \text{(During rupture propagation)} \\ 0 & \text{(After rupture arrest)} \end{cases} \tag{35}$$

The local dissipative stress τ_1 can be expressed as a Dirac δ function at $\delta_1 = 0^+$ and zero elsewhere. Then $\tau_{D\delta}$ has the same shape:

$$\tau_{D\delta}(\delta_1') = \frac{D}{2l}\delta_{\text{Dirac}}(\delta_1' - 0^+) \tag{36}$$

Figures 9(*b*) and 9(*c*) illustrate the energy partitioning diagrams for the process considered here (the actual positioning of lines,

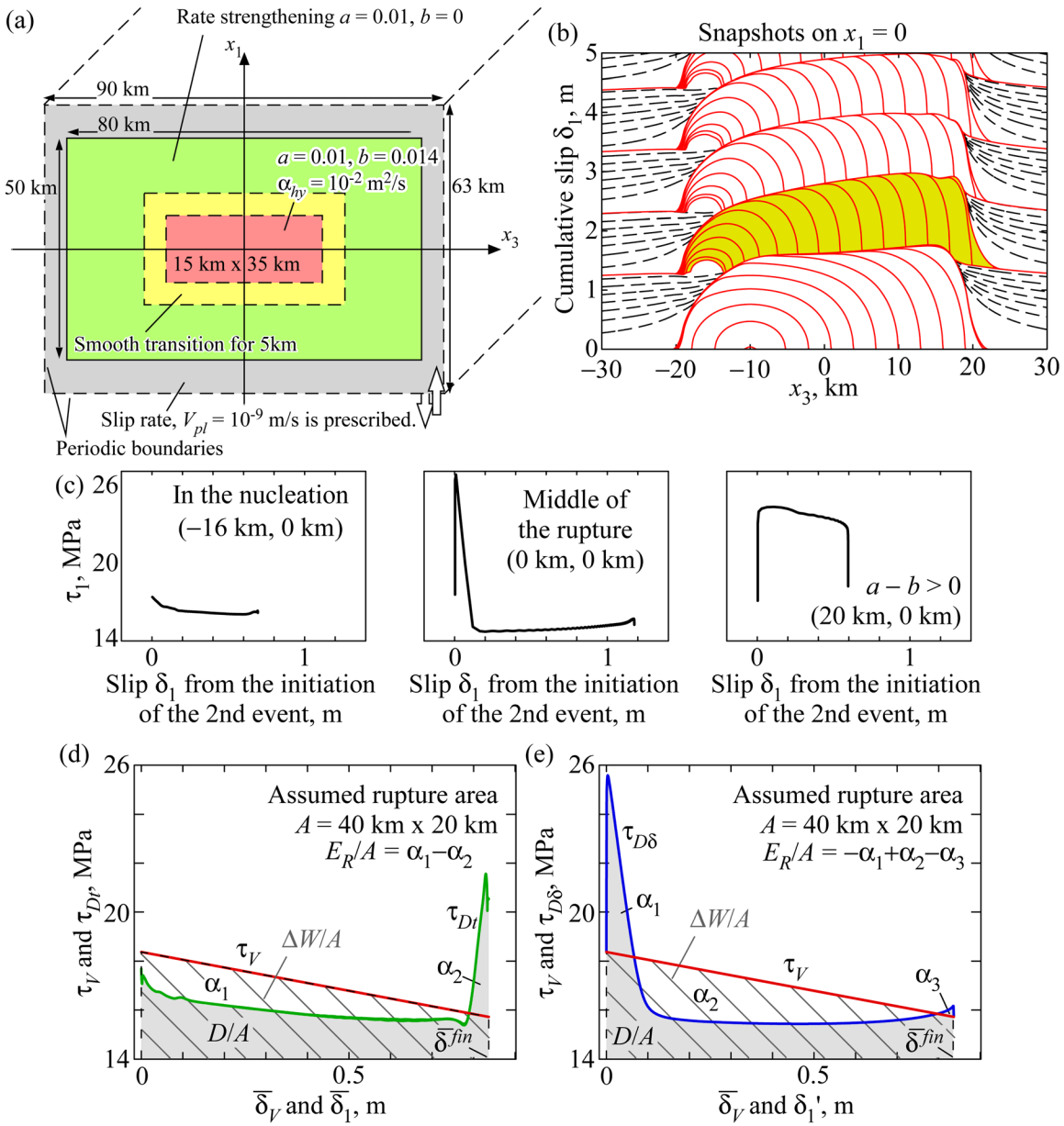

Fig. 11 Example of dynamic rupture obtained in a long-term simulation of fault slip. (*a*) Fault geometry: A seismogenic region is embedded into a stable domain, with far-field slip with 10^{-9} m/s. (*b*) Accumulation of slip along the mid-depth of the fault (axis x_3). Slow slip is shown by dashed lines plotted every 10 years and occasional fast dynamic rupture events are illustrated by solid lines plotted every 1 s for periods of high enough slip rate. (*c*) Shear stress versus slip behavior of three points along the mid-depth of the fault. The middle panel gives the behavior typical of most rupture points. (*d*)–(*e*) Rupture-averaged behavior for the event indicated by filling in (*b*).

e.g., the level of nonzero $\tau_{D\delta}$, corresponds to $v_R = 0.7c_s$). For the diagram based on $\tau_{D\delta}$ (Fig. 9(*c*)), the dissipated energy density $D/(2l)$ is the area under the Dirac δ function.

5.2 Pulse-Like Rupture due to Enhanced Weakening at High Slip Rates. Recent laboratory experiments for rock friction have revealed significant weakening of friction at coseismic slip rates of the order of 1 m/s (Refs. [7,10,13]). Such frictional behavior, combined with sufficiently low shear prestress, can lead to generation of short-duration self-healing ruptures typically called pulse-like (Refs. [16,26–28]) which may be the rupture process of choice for large earthquakes [29].

Here we consider an example of a dynamic 3D pulse-like rupture based on the SCEC/USGS Spontaneous Rupture Code Verification Project, problem TPV103 (Ref. [23]). The fault geometry is the same as in the case of Fig. 2. The main difference is in the fault constitutive relation, which combines rate-and-state friction with additional substantial weakening at seismic slip rates. Another difference with the case of Fig. 2, and with the SCEC/USGS benchmark TPV103, is how the rupture is initiated. In TPV103, the rupture is initiated by relatively fast time-dependent increase in loading. Here, we take the final distribution of that loading as the initial stress condition on the rupture domain. The other aspects of the problem are the same as in TPV103[2].

The rupture process is shown in Fig. 10(*a*). The rupture becomes pulse-like after propagating for about 5 km, and arrests after reaching the rate-strengthening barrier that surrounds the rectangular rupture domain. Figure 10(*b*) gives the evolution of shear stress at several points of the rupture. After the shear stress reaches its maximum value, weakening takes place and slip mostly occurs at much lower frictional resistance. After some increase in shear stress caused by decrease in slip rates at the end of slip, the slip stops.

The local characteristics of shear stress versus slip behavior survive the averaging procedure through $\tau_{D\delta}$ (Fig. 10(*d*)), including some increase of shear stress at the end of the rupture typically called "restrengthening." The final averaged shear stress $\tau_V\left(\bar{\delta}^{\text{fin}}\right)$ is higher than the typical one during dynamic sliding, a situation sometimes referred to as "undershoot" (e.g., Ref. [19]). The situation with the typical dynamic stress and the final stress is reversed for the rupture of Fig. 2 (Fig. 8), which would correspond to the "overshoot." Note that the rupture of Fig. 2 has relatively long slip duration in most points, comparable to the overall rupture duration. Such ruptures are typically called crack-like.

5.3 Dynamic Rupture Produced in a Long-Term Simulation of Fault Slip. As a final example, let us consider a dynamic rupture process that spontaneously occurs as a part of simulation that includes both inertially driven (seismic) and quasi-static (aseismic) slip. We consider the second event from the simulation reported in Fig. 5 of Ref. [4]. The work of Ref. [4] considered the interaction of two interface patches with different properties. However, the example we select has the same properties in both patches, so that the rupture domain is a rectangular patch of uniform rupture-promoting properties (rate-weakening friction of a rate and state type combined with a mild pore pressurization at seismic slip) embedded in a stable domain of rate-strengthening behavior (Fig. 11(*a*)). The fault is loaded by slow, tectonic-like motion further along the interface, with the imposed relative slip rate of 10^{-9} m/s in the $\boldsymbol{e_1}$ direction. The physical model is discussed in detail in Ref. [4]. The model produces a sequence of dynamic rupture events in the patch, separated in time, with slow slip in the stable part of the fault. This behavior is illustrated in Fig. 11(*b*) which shows slip accumulation along the x_3 axis passing through the mid-depth of the fault. Each dynamic rupture initiates spontaneously in the model through gradual acceleration of initially slow slip. Hence there is no need for an artificial nucleation procedure through overstressing employed in the single rupture cases of Fig. 2 and Fig. 10, which causes larger slip around the nucleation location. Let us consider the second event in the sequence, indicated by filling in Fig. 11(*b*). The local shear stress-slip behavior for several points is illustrated in Fig. 11(*c*). The panel plotted for the middle of the rupture gives the behavior typical for most points on the fault, and it is similar to the case of Sec. 5.2. The other two panels illustrate how different the behavior can be at points close to the nucleation and arrest of rupture.

The rupture-averaged quantities and the virtual work rate are plotted in Fig. 11(*d*). τ_{Dt} shows that friction dissipation sharply increases at the end of the rupture, when slip is being gradually arrested in the rate-strengthening region. At the same time, τ_{Dt} does not have the initial peak present in Figs. 2 and 10, since that peak is due to the artificial nucleation. As in the previous examples, $\tau_{D\delta}$ succeeds in capturing the shape of the most common stress-slip behavior, and can be used to study energy partitioning. Note that the end points of $\tau_{D\delta}$ and τ_V appear to coincide in Fig. 11(*d*). Based on the discussion of Sec. 4.3, this implies that the slip is mostly in $\boldsymbol{e_1}$ direction, as is the imposed loading. This case has an additional complication: since slip occurs on the fault at all times, accelerating before the dynamic rupture and decelerating after it, the initial and final stages of the rupture are not uniquely defined. We use a slip rate threshold to define the beginning and end of the rupture. The choice of the threshold slightly affects the initial and final stress, slip, and slip rate distributions, and hence the endpoints of the curves in Fig. 11(*d*). As the threshold is chosen smaller and smaller, the end points of the $\tau_{D\delta}$ and τ_V become closer and closer to each other.

6 Conclusions

We construct two functions, τ_{Dt} and $\tau_{D\delta}$, which provide an average measure of dissipative stress during dynamic rupture by describing the increment in dissipation per increment in slip, and study their properties on several examples. The first function, τ_{Dt}, reflects the evolution of the rupture process with time and hence can be used to study when significant dissipation takes place during the dynamic rupture process. However, τ_{Dt} does not resemble the local relation between frictional resistance and slip. The second one, $\tau_{D\delta}$, is specifically constructed to reflect the local behavior, and performs well in that regard for the dynamic ruptures considered. For example, it can capture large strength drop followed by re-strengthening before the rupture arrest. The proposed function $\tau_{D\delta}$, together with the virtual work rate τ_V, can be used to visualize energy partitioning during dynamic rupture in a diagram that reflects the dominant features of local friction behavior. Such diagrams have already been used in conceptual discussions [17,19], and the developments of this work provide a rigorous way for constructing them, e.g., in dynamic rupture models. The virtual work rate τ_V can be constructed as a linear function of fault-averaged slip in a virtual quasi-static process that connects the initial and final stress distributions averaged with the final slip as the weighting function. Note that the evolution of the rupture area-averaged shear stress $\bar{\tau}_1$ with area-averaged slip does not integrate to the total dissipation, and hence cannot be used to visualize the energy partitioning. Its shape is also quite different from the local friction behavior.

The dynamic rupture examples considered in this study, while variable in space and time, do not contain the level of heterogeneity sometimes inferred for natural earthquakes [30]. Investigating and visualizing energy partitioning for rupture process with heterogeneous distributions of friction constitutive parameters, which could lead to significant variations in rupture speed and multiple slip pulses, is an interesting issue for future study. It would also be important to understand how to appropriately use the rupture-averaged behavior and the associated energy-partitioning diagrams to link to laboratory observations, which may involve external energy input instead, or in addition to, the elastic strain energy stored in the apparatus (Ref. [31]).

[2]Described in detail at http://scecdata.usc.edu/cvws/.

Acknowledgment

We are pleased and honored to contribute to the volume celebrating seminal contributions of Jim Rice to mechanics in geophysical and materials sciences and gratefully acknowledge our professional and personal interactions with Jim. This study was supported by National Science Foundation (Grant No. EAR 0548277). The numerical simulations for this research were performed on Caltech Division of Geological and Planetary Sciences Dell cluster. We thank Hiroo Kanamori for insightful discussions that motivated this study.

Nomenclature

$^{\text{ini}}$ = superscript denoting the initial value of a quantity
$^{\text{fin}}$ = superscript denoting the final value of a quantity
$_{1,\,2,\,3}$ = subscripts denoting components of vector quantities
A = area of rupture domain Σ
c_s = shear wave speed
D = total dissipation in an event
D_c = slip-weakening distance
$\boldsymbol{e_1}$ = a basis vector oriented along the overall slip direction
$\boldsymbol{e_2}$ = the basis vector normal to the fault
$\boldsymbol{e_3}$ = the other basis vector in the fault plane
E_R = radiated energy
G = energy release rate during dynamic rupture propagation
G_0 = energy release rate during quasi-static rupture propagation
l = rupture half-length
P_1 = the first component of the potency vector
S = an infinite plane which includes the rupture domain Σ
t = time
t_{inv} = a function of slip defined at each point on the fault which gives the time when the slip is equal to the argument
v_R = rupture speed
w_{III} = ratio of G to G_0
W = strain energy
$\boldsymbol{x}$ = position vector
δ = slip in a system with one degree of freedom
$\boldsymbol{\delta}$ = slip vector in a dynamic rupture process
$\dot{\boldsymbol{\delta}}$ = slip rate vector
$\overline{\delta}$ = fault-averaged slip which is a function of time
$\boldsymbol{\delta}_{vp}$ = slip distribution in a virtual process
$\overline{\delta}_V$ = fault-averaged slip in a virtual process
δ_1 = an auxiliary variable representing local slip in the direction $\boldsymbol{e_1}$
δ'_1 = a slip-like quantity appearing in the definition of $\tau_{D\delta}$
$\tilde{\delta}_1$ = slip in the direction $\boldsymbol{e_1}$ normalized by its final value
δ_{Dirac} = dirac δ function
ΔW = decrease in strain energy
λ = a parameter in the interpolation between initial and final conditions
μ = shear modulus
Σ = rupture domain
$\boldsymbol{\tau}$ = shear stress on the fault
τ = shear stress in a system with one degree of freedom
$\boldsymbol{\tau}_{vp}$ = shear stress in a quasi-static virtual process
τ_V = virtual work rate
τ_D = dissipation per slip in a system with one degree of freedom
τ_{Dt} = dissipative stress in a dynamic rupture process
$\tau_{D\delta}$ = averaged shear stress-slip relation useful for energy partitioning diagrams
τ_{sc} = scalar shear stress, dissipation per slip in the direction $\boldsymbol{e_1}$
Ω = dissipation rate density $\boldsymbol{\tau} \cdot \dot{\boldsymbol{\delta}}$

References

[1] Rice, J. R., 1980, "The Mechanics of Earthquake Rupture," *Proceedings of the International School of Physics 'Enrico Fermi', Course 78*, 1979, A. M. Dziewonski and E. Boschi, eds.,Italian Physical Society and North-Holland Publishing Co., Amsterdam, pp. 555–649.
[2] Rice, J. R., 1993, "Spatio-Temporal Complexity of Slip on a Fault," J. Geophys. Res., **98**, pp. 9885–9907.
[3] Ben-Zion, Y., and Rice, J. R., 1995, "Slip Patterns and Earthquake Populations along Different Classes of Faults in Elastic Solids," J. Geophys. Res., **100**, pp. 12959–12983.
[4] Noda, H., and Lapusta, N., 2010, "Three-Dimensional Earthquake Sequence Simulations With Evolving Temperature and Pore Pressure Due to Shear Heating: Effect of Heterogeneous Hydraulic Diffusivity," J. Geophys. Res., **115**, p. B12314.
[5] Dieterich, J. H., 1979, "Modeling of Rock Friction. 1. Experimental Results and Constitutive Equations," J. Geophys. Res., **84**(B5), pp. 2161–2168.
[6] Ruina, A., 1983, "Slip Instability and State Variable Friction Laws," J. Geophys. Res., **88**, pp. 10,359–10,370.
[7] Tsutsumi, A., and Shimamoto, T., 1997, "High Velocity Frictional Properties of Gabbro," Geophys. Res. Lett., **24**, pp. 699–702.
[8] Chester, F. M., and Chester, J. S., 1998, "Ultracataclasite Structure and Friction Processes of the Punchbowl Fault, San Andreas System, California," Tectonophys., **295**, pp. 199–221.
[9] Marone, C., 1998, "Laboratory-Derived Friction Laws and their Application to Seismic Faulting," Ann. Rev. Earth Planet. Sci., **26**, pp. 643–696.
[10] Beeler, N. M., Tullis, T. E., and Goldsby, D. L., 2008, "Constitutive Relationships and Physical Basis of Fault Strength Due to Flash Heating," J. Geophys. Res., **113**, p. B01401.
[11] Noda, H., and Shimamoto, T., 2011, "Transient Behavior and Stability Analyses of Halite Shear Zones With an Empirical Rate-And-State Friction to Flow Law," J. Struct. Geol., (in press).
[12] Noda, H., Kanagawa, K., Hirose, T., and Inoue, A., 2011, "Frictional Experiments of Dolerite at Intermediate Slip Rates With Controlled Temperature: Rate Weakening or Temperature Weakening?," J. Geophys. Res., **116**, p. B07306.
[13] Rice, J. R., 2006, "Heating and Weakening of Faults During Earthquake Slip," J. Geophys. Res., **111**(B5), p. B05311.
[14] Dieterich, J. H., 2007, "Applications of Rate- and State-Dependent Friction to Models of Fault Slip and Earthquake Occurrence," *Treatise on Geophysics*, H. Kanamori, ed., Elsevier, Amsterdam, Chap. 4, pp. 107–129.
[15] Dieterich, J. H., 2007, "Friction of Rock at Earthquake Slip Rates," *Treatise on Geophysics*, H. Kanamori, ed., Elsevier, Amsterdam, Chap. 5, pp. 131–152.
[16] Noda, H., Dunham, E. M., and Rice, J. R., 2009, "Earthquake Ruptures With Thermal Weakening and the Operation of Major Faults at Low Overall Stress Levels," J. Geophys. Res., **114**, p. B07302.
[17] Kanamori, H., and Brodsky, E., 2004, "The Physics of Earthquakes," Rep. Prog. Phys., **67**(8), pp. 1429–1496.
[18] Venkataraman, A., and Kanamori, H., 2004, "Observational Constraints on the Fracture Energy of Subduction Zone Earthquakes," J. Geophys. Res., **109**, p. B05302.
[19] Kanamori, H., and Rivera, L., 2006, "Energy Partitioning During an Earthquake," *Earthquakes: Radiated Energy and the Physics of Faulting*, R. Abercrombie, A. McGarr, H. Kanamori, and G. D. Toro, eds., AGU, Washington D.C., Vol. 170, pp. 3–13.
[20] Rice, J. R., and Ruina, A. L., 1983, "Stability of Steady Frictional Slipping," J. Appl. Mech., **50**, pp. 343–349.
[21] Mitsui, Y., and Hirahara, K., 2009, "Coseismic Thermal Pressurization Can Notably Prolong Earthquake Recurrence Intervals on Weak Rate and State Friction Faults: Numerical Experiments Using Different Constitutive Equations," J. Geophys. Res., **114**, p. B09304.
[22] Day, S. M., Dalguer, L. A., Lapusta, N., and Liu, Y., 2005, "Comparison of Finite Difference and Boundary Integral Solutions to Three-Dimensional Spontaneous Rupture," J. Geophys. Res., **110**, p. B12307.
[23] Harris, R. A., Barall, M., Archuleta, R., Dunham, E. M., Aagaard, B., Ampuero, J.-P., Bhat, H., Cruz-Atienza, V., Dalguer, L., Dawson, P., Day, S., Duan, B., Ely, G., Kaneko, Y., Kase, Y., Lapusta, N., Liu, Y., Ma, S., Oglesby, D., Olsen, K., Pitarka, A., Song, S., and Templeton, E., 2009, "The SCEC/USGS Dynamic Earthquake-Rupture Code Verification Exercise," Seismol. Res. Lett., **80**(1), pp. 119–126.
[24] Kostrov, B. V., 1964, "Self Similar Problems of Propagation of Shear Cracks," J. Appl. Math. Mech., **28**, pp. 1077–1087.
[25] Broberg, K. B., 1999, *Cracks and Fracture*, Academic Press, London.
[26] Zheng, G., and Rice, J. R., 1998, "Conditions Under Which Velocity-Weakening Friction Allows a Self-Healing Versus a Crack-Like Mode of Rupture," Bull. Seismol. Soc. Am., **88**, pp. 1466–1483.
[27] Lu, X., Lapusta, N., and Rosakis, A. J., 2007, "Pulse-Like and Crack-Like Ruptures in Experiments Mimicking Crustal Earthquakes," Proc. Natl. Acad. Sci. USA, **104**, pp. 18,931–18,936.
[28] Lu, X., Lapusta, N., and Rosakis, A. J., 2010, "Rupture Modes in Laboratory Earthquakes: Effect of Fault Prestress and Nucleation Conditions," J. Geophys. Res., **115**, p. B12302.
[29] Heaton, T. H., 1990, "Evidence for and Implications of Self-Healing Pulses of Slip in Earthquake Rupture," Phys. Earth Planet. In., **64**, pp. 1–20.
[30] Lavallée, D., Liu, P., and Archuleta, R. J., 2006, "Stochastic Model of Heterogeneity in Earthquake Slip Spatial Distributions," Geophys. J. Int., **165**, pp. 622–640.
[31] Sone, H., and Shimamoto, T., 2009, "Frictional Resistance of Faults During Accelerating and Decelerating Earthquake Slip," Nature Geosci., **2**, pp. 705–708.